

# Chemistry and structure of core/double-shell nanoscale precipitates in Al–6.5Li–0.07Sc–0.02Yb (at.%)

Christian Monachon<sup>a,b</sup>, Matthew E. Krug<sup>a</sup>, David N. Seidman<sup>a,c</sup>, David C. Dunand<sup>a,\*</sup>

<sup>a</sup> Department of Materials Science and Engineering, Northwestern University, 2220 Campus Drive, Evanston, IL 60208, USA

<sup>b</sup> Swiss Federal Institute of Technology, Lausanne (EPFL), CH-1015 Lausanne, Switzerland

<sup>c</sup> Northwestern University Center for Atom-Probe Tomography (NUCAPT), 2220 Campus Drive, Evanston, IL 60208, USA

Received 6 August 2010; received in revised form 13 January 2011; accepted 8 February 2011

Available online 14 March 2011

## Abstract

An Al–6.3Li–0.07Sc–0.02Yb (at.%) alloy is subjected to a double-aging treatment to create nanoscale precipitates, which are studied by atom-probe tomography and transmission electron microscopy. After homogenization and quenching, Yb atoms form clusters exhibiting L1<sub>2</sub>-like order. A first aging step at 325 °C leads to a doubling of microhardness as a result of the formation of coherent precipitates with an Al<sub>3</sub>Yb-rich core and an Al<sub>3</sub>Sc-rich shell. The core and shell both exhibit the L1<sub>2</sub> structure and both contain a large concentration of Li, which substitutes for up to 50% of the Sc or Yb atoms at their sublattice positions. These core/single-shell precipitates provide excellent resistance to overaging at 325 °C. Subsequent aging at 170 °C increases the microhardness by an additional 30%, through precipitation of a metastable δ'-Al<sub>3</sub>Li second shell on the core/single-shell precipitates, thereby forming a chemically and structurally complex core/double-shell structure. The metastable δ'-Al<sub>3</sub>Li phase is observed to form exclusively on pre-existing core/shell precipitates.

© 2011 Acta Materialia Inc. Published by Elsevier Ltd. All rights reserved.

**Keywords:** Aluminum alloys; L1<sub>2</sub>; Precipitation strengthening; Rare earth; Scandium

## 1. Introduction

Hypoeutectic Al–Sc alloys derive their strength from a high number density of nanoscale Al<sub>3</sub>Sc precipitates with an L1<sub>2</sub> structure, which exhibit excellent resistance to coarsening to ~300 °C (~0.5 of the absolute melting point of Al) [1–13]. Dilute Al–Sc–X ternary alloys have been extensively studied, where the second alloying element X is chosen to partition either mainly to the α-Al matrix (Mg [14–20]) or to the precipitates (transition metals or lanthanoids [21–31]). Lithium is an unusual alloying element for Al–Sc alloys, since it has high solubility in the face-centered cubic (fcc) α-Al matrix [32–38] (similar to Mg) as well as in the L1<sub>2</sub> Al<sub>3</sub>Sc precipitates [39,40], which is similar to transition metals and lanthanoids, and additionally

forming metastable L1<sub>2</sub> δ'-Al<sub>3</sub>Li precipitates. Lithium additions reduce the density of Al alloys – for the present alloy, a density reduction of approximately 5% from pure aluminum to 2.567 ± 0.001 g cm<sup>-3</sup> was measured, while increasing their stiffness [41–44] and strength [33,45–56] by formation of metastable δ'-precipitates, which remain coherent up to a radius of ~200 nm due to their small lattice parameter mismatch with α-Al [57].

Whereas binary Al–Sc alloys have been investigated extensively [2,3,10,11,58], Al–Li–Sc alloys have been studied to a lesser extent. Miura et al. [59] and Krug et al. [39] used a two-step heat treatment to create Sc-rich trialuminide precipitates at high temperatures (300–350 °C), and the metastable δ'-Al<sub>3</sub>Li phase at lower temperatures (170–200 °C), which forms a shell enveloping the Al<sub>3</sub>Sc precipitates. A comparable two-step treatment was described for Al–Li–Zr alloys [60–63], where a similar Al<sub>3</sub>Zr-rich core/Al<sub>3</sub>Li-rich shell structure was achieved, using 400–600 °C

\* Corresponding author. Tel.: +1 847 491 5370; fax: +1 847 467 2269.  
E-mail address: [dunand@northwestern.edu](mailto:dunand@northwestern.edu) (D.C. Dunand).

for the  $\text{Al}_3\text{Zr}$  precipitation step, given the significantly smaller diffusivity of Zr in Al as compared to Sc [64]. Recently, Radmilovic et al. [40] and Rossel et al. [65] studied a quaternary Al–Li–Sc–Zr alloy, building upon a knowledge of the Al–Li–Zr and Al–Li–Sc ternary systems. Their first aging step was at 450 °C, where  $\text{L}_{12}$   $\text{Al}_3(\text{Li}, \text{Sc}, \text{Zr})$  precipitates form with a Zr-enrichment at the interface with the  $\alpha$ -Al matrix. During the second heat treatment at 190 °C, an additional  $\text{L}_{12}$   $\delta'$ - $\text{Al}_3\text{Li}$ -rich shell forms upon these precipitates to form core/single-shell precipitates. Although the spatial extent of Zr-enrichment is not sufficient to constitute a distinct shell, these precipitates exhibit a complex variation of concentrations from their centers to their interfaces with the  $\alpha$ -Al matrix.

In the present study, we describe a new alloy system based on Li additions to the ternary Al–Sc–Yb system. This ternary system forms core/single-shell precipitates during a single-step aging treatment with an  $\text{L}_{12}$   $\text{Al}_3\text{Yb}$ -rich core nucleating, before being enveloped by an  $\text{L}_{12}$   $\text{Al}_3\text{Sc}$ -rich shell [21]. In contrast to the Li-containing alloys, in the ternary Al–Sc–Yb system the core/single-shell structure is a result of the larger diffusivity of Yb compared to Sc at the aging temperature, 300 °C [66]. In the quaternary Al–6.3Li–0.07Sc–0.02Yb (at.%) alloy (hereafter all concentrations are in at.% unless otherwise noted), we utilize a heat treatment to create novel core/double-shell nanoscale precipitates [67]. The alloy composition was chosen with the objective of ensuring that all alloying elements are soluble in the  $\alpha$ -Al matrix during a homogenization treatment and exceed their solubility limit when aging at a lower temperature to enable the creation of precipitates. The Li concentration is also limited by the possibility of forming the stable AlLi  $\delta$ -phase with the  $\text{B}_{32}$  structure [68,69], which decreases the toughness and corrosion resistance of Al–Li alloys and also depletes the  $\alpha$ -Al matrix of Li, thereby limiting the achievable maximum volume fraction of metastable  $\delta'$ - $\text{Al}_3\text{Li}$ . This article focuses on: (i) verification that the core/single-shell precipitate structures observed in simpler ternary systems are observed with the quaternary solute additions; (ii) the effect of the Li addition on Sc precipitates in Al–Sc based alloys; and (iii) interactions among the three alloying elements.

In this article, we verify the first of the above three points. Moreover, we demonstrate that: (i) Li increases the number density of precipitates nucleated at 325 °C by a factor of  $\sim 2$ – $5$  as compared with Al–Sc or Al–Sc–Yb alloys [21], and more generally Al–Sc–RE alloys (RE = rare earth) [31] aged using similar aging conditions; (ii) Li substitutes for Sc and Yb in the  $\text{L}_{12}$  structure of the precipitates obtained after aging at 325 °C, enabling high precipitate volume fractions as compared to an Al–Sc–Mg alloy, which is the closest comparable Al–Sc alloy including an light alloying element [18]; and (iii) overaging of this alloy during an isothermal heat treatment is delayed as compared to similar alloys [18,21,22,31,34,70], suggesting that, due to the Li addition, the alloying elements have interactions that are absent in less complex alloys.

## 2. Experimental procedures

### 2.1. Aging treatments

The alloy was cast in an inductively heated furnace under three atmospheres of argon. The charge consisted of an Al–11.3Li–0.11Sc master alloy and an Al–3.7Yb master alloy (at.%) produced by arc melting. The aluminum source for the master alloys and for final dilution was Alfa Aesar, and was 99.999% pure; the master alloys were 99.9% pure. The composition of the as-cast alloy was determined to be  $6.3 \pm 0.1$  at.% Li,  $688 \pm 25$  at. ppm Sc and  $179 \pm 10$  at. ppm Yb (corresponding to 1.7 wt.% Li,  $0.12 \pm 0.004$  wt.% Sc and  $0.12 \pm 0.004$  wt.% Yb) by direct coupled plasma mass spectrometry (DCPMS), performed at Wah Chang Laboratories (Albany, OR). The heat treatment protocol consisted of the following three steps: (i) homogenization at 640 °C for 72 h in molten LiCl terminated by quenching into iced brine ( $-10$  °C); (ii) aging at 325 °C in a molten salt mixture ( $\text{NaNO}_2:\text{NaNO}_3:\text{KNO}_3$ ), followed by direct quenching into a 170 °C oil bath; and (iii) aging at 170 °C in this oil bath and then quenching in iced brine. Scanning electron microscope (SEM) observations after the 640 °C homogenization step revealed equiaxed, non-spheroidal primary precipitates of maximum dimensions  $\sim 1$ – $5$   $\mu\text{m}$ , containing Sc, Yb and Li at the grain boundaries. Consequently, the  $\alpha$ -Al matrix had a composition of Al–5.5Li–0.055Sc–0.008Yb (at.%) as measured by atom-probe tomography (APT) [71–74], performed immediately after homogenization and quenching. The first high-temperature aging treatment was performed at 325 °C to avoid the creation of the stable AlLi  $\delta$ -phase, which forms below 320 °C for binary Al–Li at this Li concentration [34] while maximizing the driving force for nucleation of the Sc and Yb-containing  $\text{L}_{12}$ -phase, thereby avoiding heterogeneous nucleation on dislocations or other imperfections. The low-temperature aging treatment occurred at 170 °C, close to the metastable  $\delta'$ - $\text{Al}_3\text{Li}$  solvus line in the Al–Li system [35], to minimize the driving force for homogeneous nucleation of metastable  $\delta'$ - $\text{Al}_3\text{Li}$  and consequently favoring heterogeneous nucleation on the pre-existing  $\text{Al}_3(\text{Sc}, \text{Yb})$  precipitates. Although it would have resulted in a higher precipitate volume fraction and number density, a temperature lower than 170 °C was not utilized, to obtain reasonably rapid precipitation kinetics. Several  $4 \times 4 \times 4$  mm<sup>3</sup> samples, subject to the above heat treatments for different aging times, were cold-mounted in an acrylic resin and polished to a 1  $\mu\text{m}$  finish using a water-based diamond suspension. Microhardness was then measured at 20 different locations in at least two grains using a 200 gf load for 10 s per indent.

### 2.2. Local electrode atom probe (LEAP) tomography and transmission electron microscopy

Rods with  $\sim 0.3 \times 0.3$  mm<sup>2</sup> cross-sections were cut by a diamond saw from the aged alloy and electropolished to an

atomically sharp microtip using a solution of 10% perchloric acid in acetic acid, followed by a solution of 2% perchloric acid in butoxyethanol, at voltages varying between 7 and 14 Vdc [75]. The microtips obtained were dissected on an atom-by-atom and atomic plane-by-atomic plane basis employing a LEAP 3000X Si tomograph (Cameca (formerly Imago Scientific Instruments), Madison, WI) at a specimen temperature of  $25 \pm 1$  K and a pulse repetition rate of 250 kHz in the voltage pulsing mode, with a pulse fraction of 16% (pulse voltage/dc steady-state voltage). This pulse fraction value was chosen because at both higher and lower values the measured solute concentrations varied significantly with pulse fraction. Employing 16%, we obtain the most reliable results for solute concentration measurements.

To make transmission electron microscope (TEM) specimens,  $\sim 250 \mu\text{m}$  thick slices were cut from the aged alloy using a diamond saw, and subsequently 3 mm diameter disks were punched out of the 250  $\mu\text{m}$  slices and then ground to an  $\sim 120 \mu\text{m}$  thickness. The  $\sim 120 \mu\text{m}$  specimens were then thinned to electron transparency employing a Struers Tenupol 5 electropolisher, using an electrolyte consisting of 1 part nitric acid to 2 parts methanol. The operating temperature and voltage were  $-30^\circ\text{C}$  (dry ice in methanol) and 12–14 Vdc. The thinned samples were examined using a Hitachi H8100 TEM in dark-field imaging mode.

Statistical measurements of the observed precipitate population, specifically volume fraction,  $\phi$ , number density,  $N_V$ , and average radius,  $\langle R \rangle$ , were obtained by different methods. The precipitates created after aging at  $325^\circ\text{C}$  were investigated by LEAP tomography. The value of  $\langle R \rangle$  was deduced from the radius of gyration of precipitates [76,77] in the direction parallel to the tip axis,  $z$ , given by a modified envelope method. Only the  $z$ -direction is taken into account because directions orthogonal to the tip axis are strongly influenced by local magnification effects and because the  $z$ -direction is calibrated accurately in all the LEAP tomographic experiments acquired by adjustment of the interplanar spacing visible in the poles to match the experimentally determined values. The formula used, which assumes a spherical precipitate morphology, is a modified Guinier radius,  $r_G = (5)^{1/2} l_{gz}$ , where  $l_{gz}$  is the radius of gyration of the precipitate in the  $z$ -direction [77]. The value of  $N_V$  was obtained by dividing the number of precipitates in each tip by the volume of the tip (given by the number of atoms multiplied by the atomic volume, taking into account a detection efficiency of 0.5). The value of  $\phi$  was determined as the ratio of the number of atoms inside the precipitates to the total number of atoms in the reconstructed volume (ignoring the small difference in the lattice parameters of the phases). For precipitates created during the low-temperature ( $170^\circ\text{C}$ ) treatment, both LEAP tomography and dark-field TEM images were obtained. An image treatment method similar to that described in Ref. [78] was applied to the images, and  $R$  and  $\phi$  were measured. Precipitate truncation due to surface effects of the thin foil (measured by equal

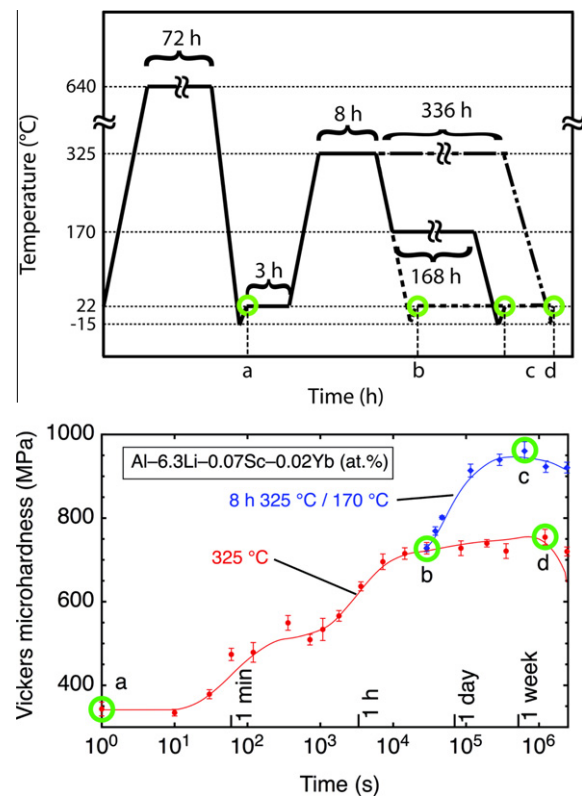


Fig. 1. (a) Schematic of aging treatment schedules; (b) microhardness aging curve for isothermal aging at  $325^\circ\text{C}$  (red circles) and isothermal aging at  $170^\circ\text{C}$  (following 8 h at  $325^\circ\text{C}$ , blue diamonds). The four states corresponding to the APT investigations (letters a–d) are circled in green in both figures.

thickness contours using the JEMS software [79]) is accounted for using the procedure described in Ref. [80]. The value of  $N_V$  is the number of precipitates in the image divided by the volume of the foil. The value of  $\phi$  is the fraction of atoms in the reconstructed volume that are contained in the precipitates, making the approximation that the lattice parameters of the  $\alpha$ -Al matrix and precipitates are identical.

### 3. Results

Fig. 1a and b displays microhardness vs. aging time and a schematic of the aging treatments utilized. For the two-step aging treatment, a time of 8 h for the  $325^\circ\text{C}$  treatment is used, leading to a peak microhardness value of  $725 \pm 10$  MPa. Table 1 compares the data obtained with existing literature values. As indicated by green circles in Fig. 1a and b, APT experiments were performed at four different stages: (a) as-homogenized state; (b and d) after a single aging step at  $325^\circ\text{C}$  for 8 and 336 h, respectively; and (c) after double aging at  $325^\circ\text{C}$  for 8 h and then at  $170^\circ\text{C}$

<sup>1</sup> For interpretation of color in all figures, the reader is referred to the web version of this article.

Table 1  
Comparison of main parameters in microhardness curves between various Al–Sc–X alloys.

Composition (at.%)	Aging temperature (°C)	Peak hardness (MPa)	Hardness plateau start (h)	End (h)
Al–0.06Sc [4,5]	300	340 ± 30	10	n.a.
Al–0.12Sc–2.0 Mg [16]	300	900 ± 30	0.5	20
Al–0.06Sc–0.005Yb [21]	300	475 ± 25	1	100
Al–0.06Sc–0.005Zr [23]	300	570 ± 40	3	220
Al–0.06Sc–0.06Ti [24]	300	420 ± 20	5	200
Al–6.5Li–0.07Sc–0.02Yb (present study)	325	710 ± 30	4	336

Table 2  
Precipitate characteristics after heat treatments.

Technique	Volume fraction $\phi$ (vol.%)	Average radius $\langle R \rangle$ (nm)	Number density $N_V$ ( $\times 10^{22} \text{ m}^{-3}$ )
<i>325 °C/8 h (treatment (b))</i>			
Core	LEAP	–	1.2 ± 0.4
Shell 1	LEAP	0.250 ± 0.005	1.9 ± 0.6
<i>325 °C/2 weeks (treatment (d))</i>			
Core	LEAP	–	2.1 ± 0.7
Shell 1	LEAP	0.293 ± 0.005	2.5 ± 0.9
<i>325 °C/8 h and 170 °C/1 week (treatment (c))</i>			
Core	LEAP	–	1.7 ± 0.5
Shell 1	LEAP	0.334 ± 0.006	2.2 ± 0.8
Shell 2	Dark-field TEM	5.5 ± 1.2	12.2 ± 0.3

for 168 h. Table 2 lists the results of measurements of the morphologies of the precipitates.

After quenching from the homogenization temperature (condition (a) in Fig. 1), the  $\alpha$ -Al matrix composition was measured by APT to be 5.5 at.% Li, 550 at. ppm Sc and 80 at. ppm Yb. Because the local solute concentration measured by APT is smaller than the bulk composition measured by DCPMS, this indicates that full homogenization of the alloy was not achieved, as confirmed by SEM observations of micrometer-sized equiaxed primary precipitates containing Sc, Yb and Li at grain boundaries. Thus, the solute concentration in the  $\alpha$ -Al matrix available for precipitation upon aging is less than the nominal composition of the alloy, and specifically the Yb/Sc ratio is 0.15 instead of the intended 0.26.

Fig. 2a displays an APT reconstruction for the homogenized and quenched state, which is characterized by the absence of visible features for the 88 million collected atoms. In Fig. 2b, the same type of reconstruction containing 80 million atoms is presented for an alloy aged for 8 h at 325 °C and Fig. 2c displays the alloy after aging at 325 °C for 8 h and at 170 °C for 1 week; it comprises 138 million atoms.

Fig. 3 is a partial radial distribution function (RDF) analysis of this dataset. An  $i$ - $X$  partial RDF [81] for the radial distance  $r$  is defined as the average concentration distribution of component  $i$  near a given solute species  $X$ ,  $\langle C_i^X(r) \rangle$  normalized to the overall concentration of  $i$  atoms,  $C_i^0$ , in the total volume considered,

$$\text{RDF}_i^X = \frac{\langle C_i^X(r) \rangle}{C_i^0} = \frac{1}{C_i^0} \sum_{k=1}^{N_X} \frac{N_i^k(r)}{N_{tot}^k(r)} \quad (1)$$

where  $N_i^k(r)$  is the number of  $i$  atoms in a radial shell of radius  $r$  around the  $k$ th  $X$  atom that is at the center of the shell,  $N_{tot}^k$  is the total number of atoms in this shell and  $N_X$  is the number of  $X$  atoms in the volume considered. The average concentration distributions around a solute species in 0.1-nm-thick shells are smoothed using a Gaussian-type spline function [82], with a 0.04 nm full width at half maximum, where  $\langle N_{tot}(r) \rangle$  increases quadratically with  $r$  and the total volume sampled is proportional to  $X$ . RDF $_i^X$  values of unity describe perfectly random distributions, while values that differ describe clustering or ordering. The absolute magnitude of these processes can be compared with the RDF's amplitude,  $A_i^X(r) = [\text{RDF}_i^X(r) - 1]$ .  $A_i^X(r) > 0$  indicates that, at a distance  $r$  from  $X$  atoms, the concentration of  $i$  is greater than in the overall analyzed volume (positive correlation);  $A_i^X(r) < 0$  implies that, at a distance  $r$  from  $X$  atoms, the concentration of  $i$  is smaller than in the overall analyzed volume (negative correlation).

Fig. 4 displays a single precipitate extracted from the dataset shown in Fig. 2b (aged at 325 °C for 8 h), and Fig. 5 features a proximity histogram centered on the inflection point of the Sc concentration profile for the precipitates obtained (Fig. 2b). The image in Fig. 4 is taken along a {100} family of planes in a pole of the reconstructed dataset. The reconstructed precipitate is extracted from the original dataset by using an isoconcentration surface [77,83] at the inflection point of the Sc concentration of the proximity histogram [82], as shown in Fig. 5.

Fig. 6a and b displays Li-centered partial RDFs for the two phases isolated from the same dataset, which was obtained from a specimen aged at 325 °C: Fig. 6a is for a  $2 \times 10^6$  atom dataset consisting of 32 core/shell  $\alpha'$ -Al<sub>3</sub>(Sc,

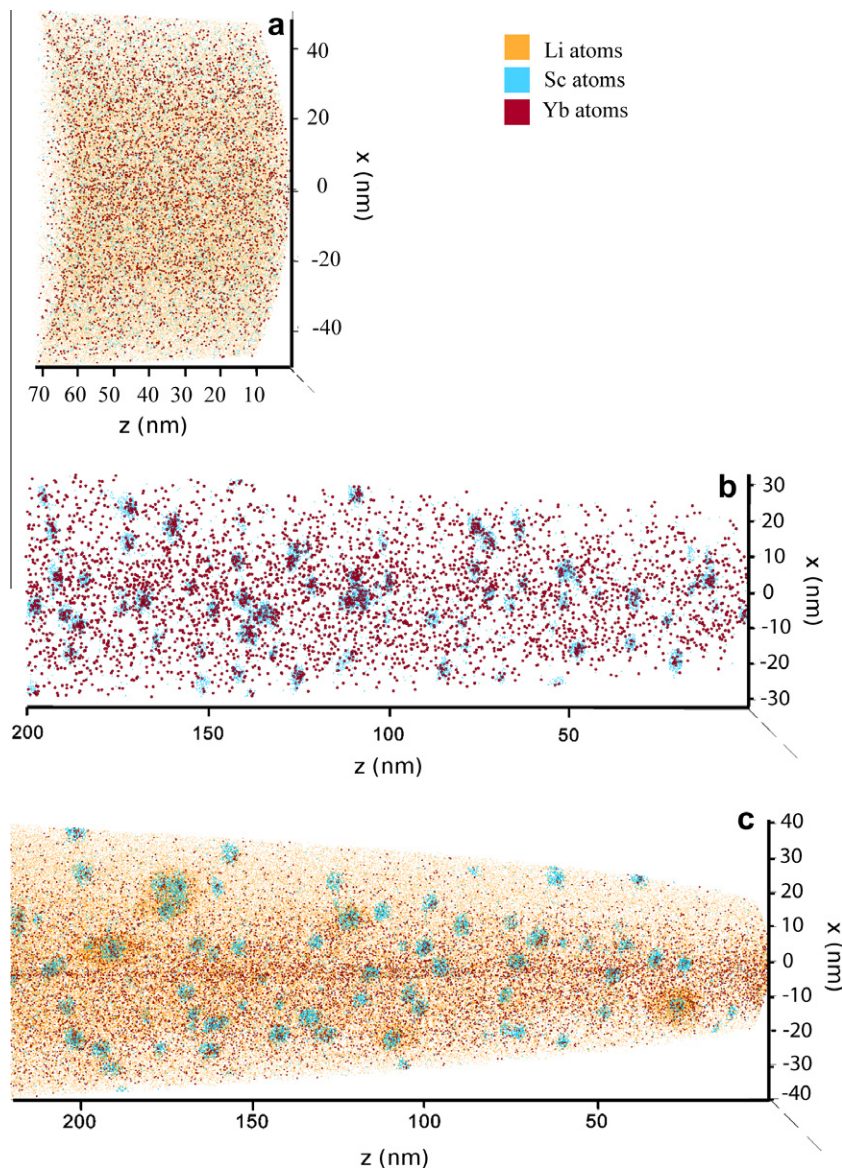


Fig. 2. Elemental LEAP tomographic reconstructions obtained after homogenization, quenching and the following aging treatments: (a) no aging; (b) aged at 325 °C for 8 h; and (c) aged at 325 °C for 8 h and at 170 °C for 1 week. In (b), Li atoms are not shown for the purpose of clarity. Condition (d) is not shown because it is very similar to condition (c).

Yb, Li) precipitates, which were isolated from the  $\alpha$ -Al matrix (case I); and Fig. 6b is for a  $10^7$  atom dataset consisting of the  $\alpha$ -Al phase from which the precipitates have been removed using the atom probe tomography analysis software program IVAS (Cameca) (case II). This separation provides useful information when considering correlations among Li atoms and the three other elements present in the alloy.

Fig. 7 displays a reconstructed core/double-shell precipitate, and a concentration profile taken through its centroid along the axis of the APT specimen for an alloy aged for 8 h at 325 °C and 1 week at 170 °C. Fig. 8 shows typical concentration profiles recorded similarly for all aging conditions studied: condition b, 8 h at 325 °C; condition c, 8 h at 325 °C and 1 week at 170 °C; and condition d, 2 weeks at 325 °C. A concentration profile is employed rather than a

proximity histogram because the shell thicknesses vary from precipitate-to-precipitate [40]. The use of a proximity histogram causes, because of the variability in shell thickness, an artificial decrease in interface abruptness, which precludes a clear observation of the core/shell structures. When compared to the proximity histogram, Fig. 5 (representing an average concentration profile for 317 precipitates), the individual concentration profile in Fig. 8b for a single precipitate has the advantage of displaying an interface's sharpness and a precipitate's dimensions, which are more accurate because, compared to the  $x$ - and  $y$ -directions (directions orthogonal to the APT tip axis), the  $z$ -direction for this profile is less affected by local magnification effects. Because measuring individual precipitates with concentration profiles results in a decrease in statistical confidence compared to measuring all precipitates in a dataset with

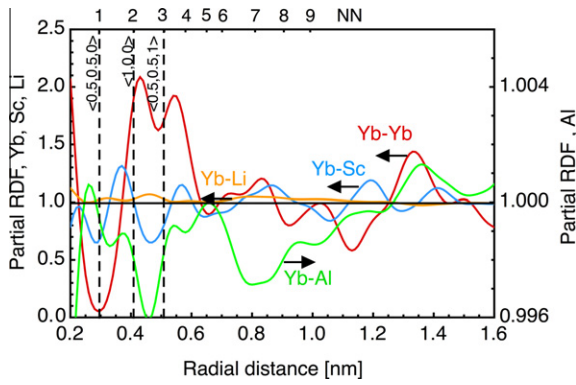


Fig. 3. Partial radial distribution function centered on Yb atoms. The sample is homogenized and quenched (condition (a)). Interplanar distances for a  $\text{Al}_3\text{Yb}$  unit cell (0.42 nm) are shown labeled by their corresponding crystallographic directions.

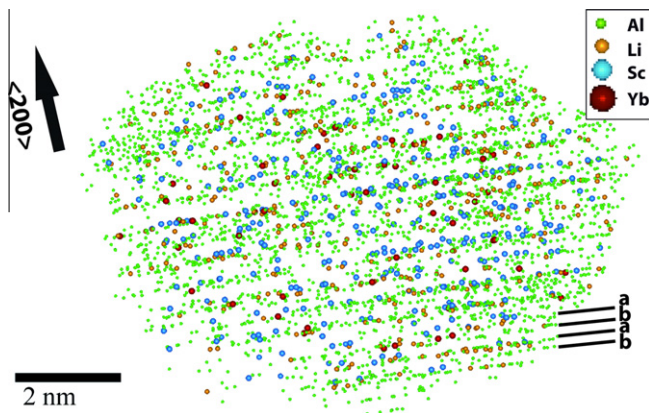


Fig. 4. Image of a precipitate delineated with an isoconcentration surface centered on the inflection point in the Sc concentration in the corresponding proxigram (Fig. 5). The precipitate is imaged along a  $\langle 200 \rangle$  zone axis visible as a low-index pole in the APT reconstruction, allowing the observation of crystallographic planes. The structure shows alternatively (a) Al-rich and (b) Al-poor planes, suggesting an  $\text{L1}_2$  structure, which is otherwise invisible in dark-field TEM due to a structure factor extinction effect.

the proxigrams method, concentration profiles were determined for at least a dozen precipitates, confirming that the results shown in Figs. 8a–c are indeed representative. These profiles are recorded along the microtip's evaporation direction, which is calibrated using interplanar spacing measurements for the low-index poles ( $\{100\}$ ,  $\{110\}$ ,  $\{111\}$  and  $\{311\}$ ). This procedure reduces the sensitivity of the concentration determination to local magnification effects.

## 4. Discussion

### 4.1. Microhardness-aging behavior

The strengthening mechanisms in the present alloy are complex, as their origins include contributions from solutes dissolved in the  $\alpha$ -Al matrix, precipitation strength-

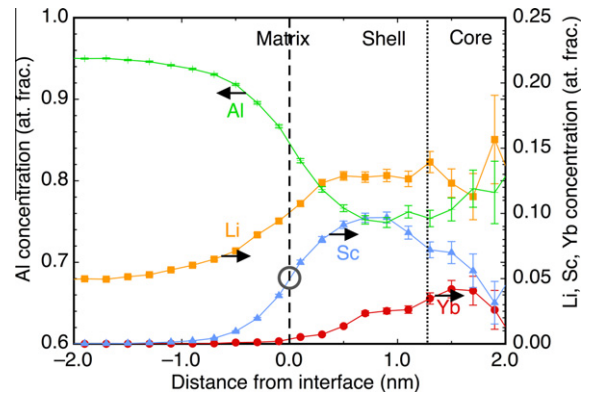


Fig. 5. Proxigram for aging condition (b) (8 h at 325 °C), based on 89 precipitates in a 22 million atom dataset. The core/shell structure is visible in spite of the interface spreading due to the variable thickness of the Sc-rich shell. The thick gray circle shows the interface position at the inflection point in the Sc concentration.

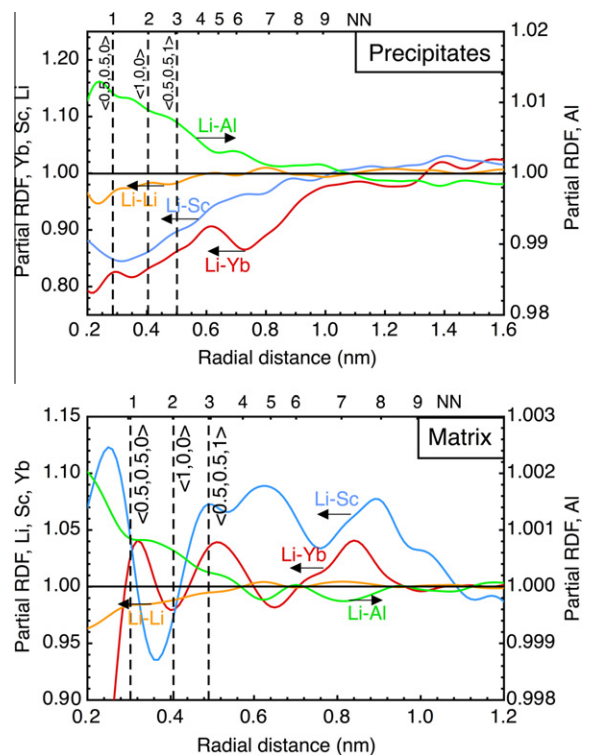


Fig. 6. Partial radial distribution functions centered on Li atoms, applied to (a) precipitates and (b)  $\alpha$ -Al matrix of a dataset obtained from a sample aged at 325 °C for 8 h (aging treatment condition (b)). The line at the value unity is the average normalized concentration of the element. The vertical dashed lines are the first-NN distances through third-NN distances and are labeled with their corresponding atomic position in the  $\text{Al}_3\text{Li}$  unit cell, from Ref. [93].

ening from the  $\alpha'$ - $\text{Al}_3(\text{Li}, \text{Sc}, \text{Yb})$  precipitates formed at 325 °C, and finally from metastable  $\delta'$ - $\text{Al}_3\text{Li}$  precipitates formed at 170 °C. The most significant contribution to solid-solution strengthening in this alloy is from Li, as it has the highest concentration of all the solutes. Strengthening in the as-quenched state is also due to the rapid

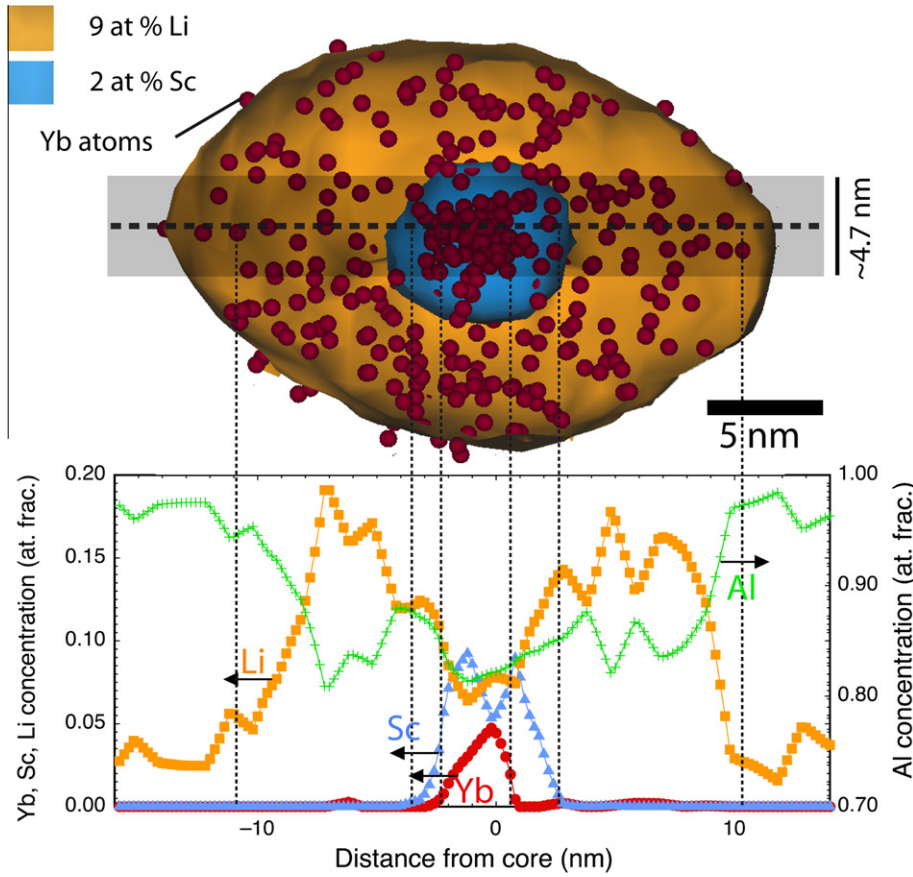


Fig. 7. A typical example among the 12 core/double-shell precipitates obtained in the APT datasets collected during this study for the case (c) aging protocol: 8 h at 325 °C followed by 2 weeks at 170 °C. The horizontal line indicates the direction of the microtip's axis. The precipitate dimensions in the  $x$ - and  $y$ -directions (in-plane and vertical in this figure) suffer an inverse magnification effect and this is not taken into account for the size measurement.

decomposition of the supersaturated Al–Li solid solution, which occurs during quenching in Al–Li alloys for an Li-concentration greater than  $\sim 6$  at.% [54]. In this research, the microhardness of the as-quenched state was determined to be  $339 \pm 12$  MPa. This is comparable to the as-solutionized and quenched hardness values of similar simpler alloys [84]: 360 MPa for Al–5.5Li and 450 MPa for Al–6.5Li (at.%), and 220 MPa for binary hypoeutectic Al–Sc alloys [23,58].

The 325 °C aging curve (Fig. 1b) displays an initial peak after 1 h of aging. A similar result is reported by van Dalen et al. [21] for a ternary Al–Sc–Yb alloy because Yb atoms cluster prior to forming  $L1_2$   $Al_3(Yb, Sc)$  precipitates. A plateau with a peak value of  $716 \pm 28$  MPa is observed after  $\sim 8$  h. The isothermal aging behavior at 325 °C (Fig. 1b) differs in many respects from prior studies performed on dilute Al–Sc, Al–Sc–Mg and Al–Sc–Yb alloys. Table 1 demonstrates the following: (i) peak (plateau) microhardness values for the binary Al–Sc or ternary Al–Sc–Yb alloys are smaller than for the present alloy; (ii) for a composition similar to the ternary Al–Sc–Yb system, the present alloy exhibits an approximately fourfold increase in the initial and final times of the microhardness plateau, despite a higher aging temperature and slightly larger Sc plus Yb concentrations; and (iii) the Al–Sc–Mg alloy reaches a

higher peak microhardness value because of the higher Sc concentration but displays a more rapid decrease in microhardness due to over aging, which commences after 20 h in Al–Sc–Mg, compared to 336 h in the present alloy.

The present alloy (Al–6.3Li–0.07Sc–0.02Yb, at.%) subjected to the two-step aging treatment (325 °C for 8 h followed by 170 °C for 1 week) achieves a microhardness of  $952 \pm 49$  MPa, which is smaller than the value ( $1320 \pm 70$  MPa) measured by Miura et al. [59]. This is explained by the higher total solute content of the alloy used by Miura et al.: 8.7 and 0.11 at.% for Li and Sc, respectively. We employed a smaller Li concentration and a lower second aging-step temperature (170 vs. 200 °C used by Miura et al.), which increases the aging time necessary to achieve peak microhardness.

Theoretical models of the strengthening of alloys due to precipitates have been extensively developed [85–87]. In the case of coherent and ordered misfitting precipitates, the strength of an alloy can be related to different dislocation interactions with precipitates and their associated strain fields. These include order strengthening, modulus and coherency mismatch strengthening, and Orowan strengthening or dislocation looping. Following Refs. [23,58], the strength increment for dislocation–precipitate interactions by order strengthening, coherency and modulus

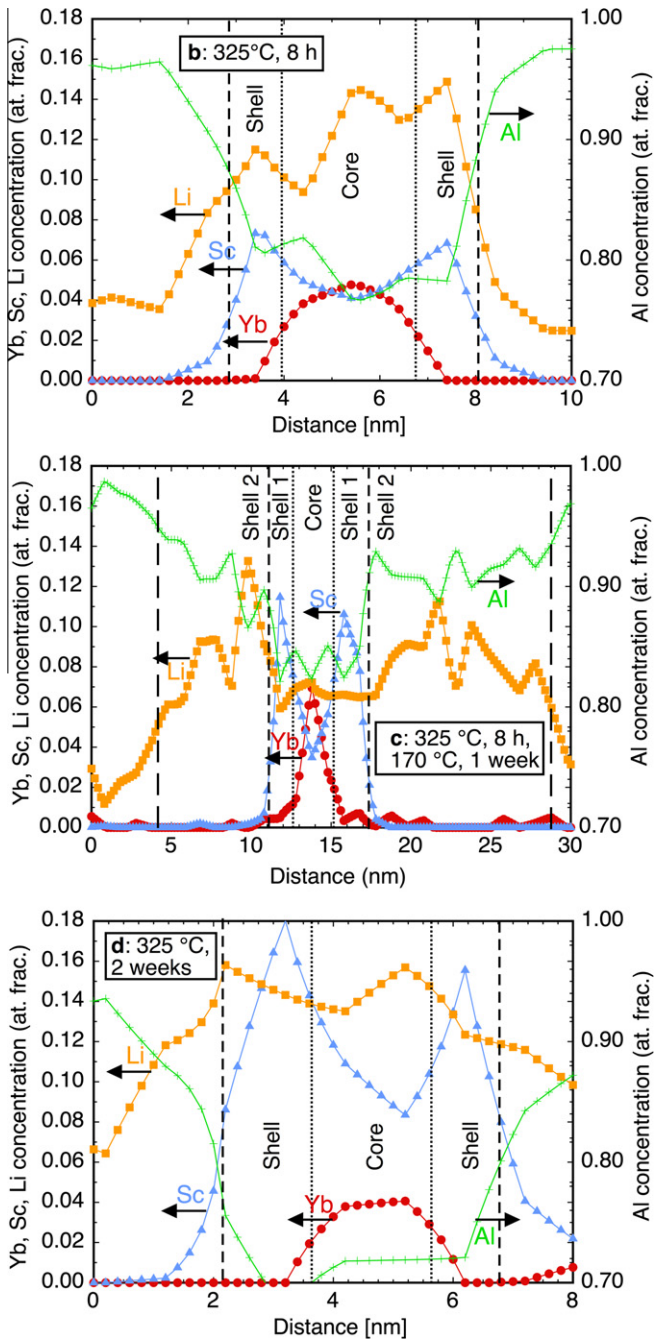


Fig. 8. Concentration profiles along the field-evaporation direction of a representative example of a precipitate obtained for aging conditions (b) 325 °C, 8 h; (c) 325 °C, 8 h, 170 °C, 1 week; and (d) 325 °C, 2 weeks respectively. Li concentration in the outer shell of case (c) suffers a measurement artifact, and is thus qualitative.

strengthening, or strengthening by the Orowan bypass mechanism are compared with the experimental strength increment, estimated as  $\Delta HV/3$  (where  $\Delta HV$  is the increase in microhardness from the as-quenched state to the aged state). For the precipitates formed after aging 8 h at 325 °C, and also for the precipitates formed after 170 °C, precipitate shearing is expected to be the active strengthening mechanism and the strengthening increments from the

two precipitation events appear to be linearly additive. We are continuing to study strengthening in these complex alloys in detail with a combined experimental and computational approach using dislocation dynamics simulations [88].

## 4.2. Microstructure evolution

### 4.2.1. Early nucleation stages

First, we make a general remark concerning datasets containing precipitates (conditions (b–d) in Fig. 1). APT data taken from samples containing nanometer-sized precipitates exhibit a local magnification effect [77,89,90] (the precipitate dimensions in directions orthogonal to the microtip axis are artificially enlarged) for the precipitates created during the 325 °C aging. In contrast, an inverse local magnification effect (the precipitate dimensions in directions orthogonal to the microtip axis are artificially diminished) is observed for the metastable  $\delta'$ -Al<sub>3</sub>Li precipitates after aging at 170 °C (condition (c) only). Additionally, the overall Li concentration decreases for condition (c), suggesting that Al<sub>3</sub>Li has a field-evaporation behavior different from that of the  $\alpha$ -Al matrix [51].

In the case of the as-quenched alloy, the Yb–Yb partial RDF,  $RDF_{Yb}^{Yb}$ , in Fig. 3 has a value less than unity ( $RDF_{Yb}^{Yb} < 1$ ) for the first nearest-neighbor (NN) distance ( $(\frac{1}{2}\frac{1}{2}0)$  vectors in an L<sub>1</sub> structure), and has a value greater than unity ( $RDF_{Yb}^{Yb} > 1$ ) for the second- and third-NN positions ( $(110)$  and  $(\frac{1}{2}\frac{1}{2}1)$  vectors). The good match between the two expected interplanar distances (Fig. 3) and the magnitudes of the correlations suggests that there is L<sub>1</sub> ordering of Yb atoms in the as-quenched state [81]. Moreover, values greater than unity for partial  $RDF_{Yb}^{Li}$  and  $RDF_{Yb}^{Al}$  at the first-NN distance suggests that Li and Al may reside on the Al sublattice of the L<sub>1</sub> structure. This partial RDF trend is less visible for Li because the normalization concentration  $C_i^0$  is close to  $\langle C_i^X(r) \rangle$ , due to the large number of atoms in the  $\alpha$ -Al matrix. A discussion of this aspect of partial RDF analysis is given in Ref. [81].

### 4.2.2. Chemical compositions of precipitates

For aging condition (b) (8 h at 325 °C), a high number density of Li-rich precipitates (Figs. 2b and 4) containing Sc and Yb is observed. Fig. 5 demonstrates that the cores and shells of these precipitates are enriched in Yb and Sc, respectively. For the two datasets collected, 80 million atoms, 317 Sc-rich precipitates with the composition Al<sub>0.800</sub>(Li<sub>0.120</sub>Yb<sub>0.027</sub>Sc<sub>0.053</sub>) and 321 Yb-rich cores with the composition Al<sub>0.780</sub>(Li<sub>0.130</sub>Yb<sub>0.048</sub>Sc<sub>0.042</sub>) were analyzed independently by the envelope method: for the Sc cluster search, a distance of 1.4 nm and a minimum number of atoms of 20 is specified, whereas for Yb, the minimum number of atoms is reduced to four [76]. By comparing the spatial coordinates of the precipitates, it is verified that all Sc-rich shells contain an Yb-rich core. The small discrepancy between the two precipitate numbers (321 Yb-rich cores compared to the 317 Sc-rich shells) is attributed

to the low threshold of 4 atoms used for Yb, which is necessary due to the small Yb concentration. For the Sc-rich precipitates, the number of precipitates analyzed by the envelope method is verified using an isoconcentration surface calculation with the inflection point in the Sc concentration profile of the corresponding proximity histogram (or proxigram) [82]; the technique consists of plotting the atomic concentration profile measured by APT as a function of distance with respect to an isoconcentration surface (Fig. 5). When this procedure is finished, counting the number of distinct isoconcentration surfaces yields the number of precipitates. As shown in Fig. 8d, the core/shell structure is also obtained for the longer aging time at 325 °C (2 weeks, heat treatment case (d)), indicating that this core/shell structure is stable at 325 °C for at least 2 weeks. The proxigram in Fig. 5 exhibits Li partitioning to the core and inner shell of the precipitate, with the partitioning coefficient,  $K_L^{ppt/matrix}$ , ranging from 2.4 to 3.2. The average composition of precipitates produced at 325 °C is  $\text{Al}_3(\text{Li}_{0.57}\text{Sc}_{0.33}\text{Yb}_{0.10})$ , but the Li concentration may be underestimated if the Li-containing phases exhibit a different field-evaporation behavior during the LEAP tomographic analyses compared to the  $\alpha$ -Al matrix [51,90]. The large amount of substitution in these precipitates demonstrates that two-thirds of the more expensive Sc can be replaced with less expensive Yb and Li while maintaining the  $\text{L1}_2$  structure, high number density and strong resistance of the precipitates to coarsening. The  $\text{L1}_2$  structure is visible in Fig. 4, where the precipitate is imaged along a  $\langle 200 \rangle$  zone axis (visible as a pole in the APT reconstruction [18]), allowing the observation of crystallographic planes. The  $\{200\}$  planes are alternatively Al-rich and Al-poor (marked (a) and (b) in Fig. 4), as anticipated for the  $\text{L1}_2$  structure.

#### 4.2.3. The structure of the precipitates

Fig. 6a demonstrates that, for precipitates formed at 325 °C for 8 h (i.e. excluding the  $\alpha$ -Al matrix), the values less than unity of the Li partial RDFs ( $\text{RDF}_{\text{Li}}^X < 1$ ) with all solute elements and the value greater than unity of the Li partial RDF with Al ( $\text{RDF}_{\text{Li}}^{\text{Al}} > 1$ ) at the first-NN distance (the distance with the highest degree of certainty for RDFs in fcc-related structures [33,34,81]) suggest an  $\text{L1}_2$  structure with Li, Sc and Yb sharing the X sites in the  $\text{Al}_3\text{X}$  structure. This observation is confirmed by direct observation of a precipitate in the region of a 200 pole in an APT dataset (Fig. 4), which provides structural information that is unavailable using TEM, as the  $\langle 100 \rangle$  type superlattice reflection is extinct for precipitates with the measured composition [62,63].

#### 4.2.4. Solute behavior in the $\alpha$ -Al matrix

For the  $\alpha$ -Al matrix (Fig. 6b), Li-centered partial RDFs are different from those displayed in Fig. 6a. A value smaller than unity for the partial RDF of Li with itself at the first-NN position ( $\text{RDF}_{\text{Li}}^{\text{Li}} < 1$ ) suggests  $\text{L1}_2$  ordering (caused by short-range diffusion of Li atoms), as observed

by Schmitz et al. [45,46], with Sc and Yb having partial RDFs with Li greater than unity. Thus, in the  $\alpha$ -Al matrix, the first-NN sites around Sc or Yb solute atoms are more likely to be occupied by Li atoms than for the case of a random solid solution. This suggests that a chemical affinity exists between Sc and Li atoms, and between Yb and Li atoms when these solutes are dissolved in the  $\alpha$ -Al matrix, possibly resulting in diffusion of Li–Sc and Li–Yb dimers via a vacancy mechanism. We cannot prove this diffusion mechanism hypothesis, but it would provide an explanation for the resistance to overaging of our alloy, which is similarly observed by Miura et al. [59]. At 325 °C Yb and Li have isotope diffusivities in pure Al that are larger by about three orders of magnitude than that of Sc in Al [64,66,91], yet by alloying Al–Sc with Yb and Li, which diffuse faster in pure Al than does Sc, the coarsening rate of Sc-containing precipitates is reduced. Solute interactions may also play a role in the difference in Yb clustering behavior between the Al–Sc–Yb alloy [21], where pure Yb clusters are found, and the present study, where nuclei with an  $\text{L1}_2$  structure are observed. Fig. 3 demonstrates that Yb–Sc and Yb–Yb partial RDFs are less than unity ( $\text{RDF}_{\text{Yb}}^{\text{Yb,Sc}} < 1$ ) and those of Yb–Al and Yb–Li are greater than unity ( $\text{RDF}_{\text{Yb}}^{\text{Al,Li}} > 1$ ) at the first-NN distance, and the Yb–Yb partial RDF is strongly greater than unity at the second-NN distance ( $\text{RDF}_{\text{Yb}}^{\text{Yb}} > 1$ ), suggesting  $\text{L1}_2$ -like short-range ordering [81].

#### 4.2.5. Core/double-shell precipitate characteristics

Aging condition (c) (double aging at 325 °C for 8 h and then at 170 °C for 1 week) results in precipitates with an  $\text{Al}_{0.833}(\text{Li}_{0.070}\text{Yb}_{0.052}\text{Sc}_{0.045})$  core, a first  $\text{Al}_{0.832}(\text{Li}_{0.090}\text{Sc}_{0.063}\text{Yb}_{0.015})$  shell and a second, outer shell with approximate  $\text{Al}_3\text{Li}$  stoichiometry. A representative example of a core/double-shell precipitate is displayed in Fig. 7, showing an APT reconstruction and a concentration profile through the precipitate, in a direction parallel to the evaporation direction: the orthogonal two axes of the profile are contracted due to an inverse magnification effect.

For the  $1.3 \times 10^8$  atoms collected, 12 core/double-shell precipitates were analyzed. Because the initial precipitates created during the first aging step at 325 °C may have further evolved during the subsequent 170 °C aging treatment, direct comparison with case (b) (aging at 325 °C for 8 h) is difficult. It is clear, however, that only a small fraction (~1 out of 15) of the initial high-temperature precipitates are enveloped by the second shell, which is formed at 170 °C. Moreover, no evidence was found for metastable  $\delta'$ - $\text{Al}_3\text{Li}$ -rich precipitates without cores, suggesting that for the small undercooling employed at 170 °C,  $\cong 30$  °C, there is insufficient thermodynamic driving force for homogeneous nucleation of the metastable  $\delta'$ - $\text{Al}_3\text{Li}$ -rich phase, which instead precipitates on the pre-existing  $\text{Al}_3(\text{Li}_{0.57}\text{Sc}_{0.33}\text{Yb}_{0.10})$  precipitates nucleated at 325 °C. This is analogous to the case of a binary Al–8.2Li (at.%) alloy, for which undercoolings smaller than 40 °C result in heterogeneous nucleation of metastable  $\delta'$ - $\text{Al}_3\text{Li}$  precipitates on

dislocations [33]. Calculations similar to those of Refs. [8,57] indicate that coherency of  $\delta'$ -Al<sub>3</sub>Li is expected for precipitate radii up to  $\sim 200$  nm.  $\delta'$ -Al<sub>3</sub>Li precipitates in the peak-double-aged state (1 week at 170 °C) have an average radius of  $12.2 \pm 0.3$  nm (Table 2); they are therefore expected to be coherent.

#### 4.3. Comparison between the performed aging treatments

Fig. 8b–d displays representative APT concentration profiles along the evaporation direction of precipitates observed after heat treatment (b, 325 °C for 8 h; c, 325 °C for 8 h plus 170 °C for 1 week; and d, 325 °C for 2 weeks). When compared to case (b), the second aging treatment at 170 °C for 1 week (case (c)) does not change the concentrations in the core and first shell significantly, and therefore this profile is treated as representative of the core/shell structure observed for aging at 325 °C. The concentration profiles (Fig. 8b–d) exhibit Li concentration of 13–17 at.% for the precipitates nucleated at 325 °C with an Al<sub>3</sub>Yb-rich core and an Al<sub>3</sub>Sc-rich first shell. This result cannot be predicted employing binary phase diagrams, and the quaternary phase diagram for this system does not exist. Indeed, the metastable  $\delta'$ -Al<sub>3</sub>Li phase is stable only below 200 °C for a binary Al–6.3Li alloy (at.%) [35,70], but for our quaternary alloy we measure 13–17 at.% Li for the peak concentration in the core/shell precipitates formed at 325 °C with Li substituting on the X sites of the L1<sub>2</sub> Al<sub>3</sub>X structure (Figs. 4–6). Peak concentrations of 4–6 Yb and 7–9 Sc (at.%) are present in the core and the first, inner shell, respectively. The Li concentration in the second, outer shell is underestimated, again because of the inverse magnification effect.

Table 2 summarizes the  $\langle R \rangle$  and  $N_V$  values of precipitates as measured by TEM and APT. Li-rich precipitates formed at 325 °C, 8 h of aging, contain a Yb-rich core and an Sc-rich outer shell with  $\langle R \rangle = 1.9 \pm 0.6$  nm, which is smaller than that found in an Al–0.054Sc–0.004Yb (at.%) alloy aged at 300 °C for 24 h ( $\langle R \rangle = 3.4 \pm 0.7$  nm) [21]. Additionally, for precipitates nucleated at 325 °C,  $N_V$  is a factor of 9 greater, and  $\phi$  is a factor of 2 greater than for precipitates nucleated at 300 °C in [21]. This large value of  $\phi$  and small value of  $\langle R \rangle$  after 2 weeks of aging at 325 °C are responsible for the microhardness remaining nearly constant at  $\sim 750$  MPa. Although the microhardness plateau for this alloy aged at 325 °C commences at a shorter time than that of Al–0.06Sc (at.%) aged at 300 °C [15,58], it has a longer duration. The same observation obtains for Al–0.06Sc–0.005X (X = Yb or Gd, at.%) aged at 300 °C [21]. Two explanations are proposed for this improved coarsening resistance.

First, the homogeneous nucleation current (number of stable nuclei per unit volume per unit time) of precipitates at 325 °C may be increased by the Li addition because it reduces the net reversible work to make a critical size nucleus,  $W^* \approx (16\pi\sigma_{int}^3)/(3(\Delta F_V)^2)$  [92], where  $\sigma_{int}$  is the interfacial free energy between the two phases and  $\Delta F_V$  is

the volume Helmholtz free energy due to the supersaturation at 325 °C. Thus, the improvement may be linked to a decrease in  $\sigma_{int}$  and/or an increase in  $\Delta F_V$  as a result of Li substitution in the precipitates. Furthermore, the driving force for nucleation in Li-containing Al–Li–Sc–RE alloys is anticipated to be larger than that of Li-free Al–Sc–RE alloys with the same Sc and Yb concentrations in the supersaturated matrix.

Second, correlated diffusion may occur between Li and Sc (and/or Li and Yb), as discussed in connection with Fig. 6, which could potentially decrease the intrinsic diffusivity coefficients of the solutes in the  $\alpha$ -Al matrix. Similarly, a reduction in the coarsening rate of metastable  $\delta'$ -Al<sub>3</sub>Li precipitates by alloying with Sc has been observed by Miura et al. [59] in an Al–8.7Li–0.11Sc (at.%) alloy. First-principles calculations of the interactions between Li, other solute elements and vacancies, and the different phases' interfacial free energies and substitutional enthalpies would help to shed light on these issues, which ultimately control the microhardness retention for the long aging times observed. In this respect, Li differs from Mg [16], which does not yield significantly different aging behavior aside from its contribution to the increased microhardness by a solid-solution strengthening mechanism. As a result, Li is an interesting light element addition to an Al–Sc alloy to obtain a coarsening resistant alloy for use at elevated temperatures.

## 5. Summary and conclusions

An Al–6.3 at.% Li alloy microalloyed with 0.07 at.% Sc and 0.02 at.% Yb was subjected to a two-step aging treatment and studied employing APT and TEM with the following results:

- Aging the homogenized  $\alpha$ -Al matrix at 325 °C results in a high number density ( $11.9 \times 10^{22} \text{ m}^{-3}$  after 8 h) of coherent, nanosized  $\alpha$ -Al<sub>3</sub>(Li<sub>0.57</sub>Sc<sub>0.33</sub>Yb<sub>0.10</sub>) precipitates.
- These precipitates exhibit a Yb-rich core and an Sc-rich outer first shell. They exhibit good stability, in terms of mean radius and chemical composition, upon long-term aging (up to 2 weeks) at 325 °C, with a concomitant retention of a microhardness value of 750 MPa. Thus, Li is an excellent candidate to replace partially the more expensive element Sc in Al–Sc based alloys.
- A second aging treatment at 170 °C leads to the heterogeneous precipitation of a second metastable  $\delta'$ -Al<sub>3</sub>Li shell upon approximately 1 in 15 of the precipitates created at 325 °C. To our knowledge, this is the first metallic alloy in which core/double-shell precipitates are formed by a scientifically designed solid-state processing protocol.
- A high microhardness value of  $725 \pm 10$  MPa is achieved after the first aging treatment at 325 °C, which is a result of the high precipitate number density ( $1.2 \times 10^{23} \text{ m}^{-3}$  after aging at 325 °C for 8 h), as compared to other studies on Al–Sc and Al–Sc–X alloys (where X = Zr, Mg, Li, Ti or rare earths).

– Also contributing to the microhardness increase are solid-solution strengthening and an increased volume fraction of the 325 °C phase, both due to the Li addition. The second aging treatment further increases the microhardness to  $952 \pm 49$  MPa by increasing the precipitate volume fraction through formation of a metastable  $\delta'$ -Al<sub>3</sub>Li outer shell on the first shell.

## Acknowledgements

The authors are grateful to Prof. A. Mortensen (EPFL, Switzerland) for co-advising C.M.'s EPFL MS thesis at Northwestern University. This research is supported by the United States Department of Energy (Basic Energy Science, Dr. J. Vetrano monitor) through Grant DE-FG02-98ER45721. The LEAP tomograph was purchased with funding from the NSF-MRI (Grant DMR-0420532) and ONR-DURIP (Grant N00014-0400798) Programs, Dr. Julie Christodoulou, grant officer.

## References

- [1] Røyset J, Ryum N. *Int Mater Rev* 2005;50:19.
- [2] Toporovan LS, Eskin DG, Kharakterova ML, Dobatkina TB. *Advanced aluminum alloys containing scandium*. Amsterdam: Gordon & Breach; 1998.
- [3] Marquis EA, Seidman DN. *Acta Mater* 2001;49:1909.
- [4] Seidman DN, Marquis EA, Dunand DC. *Acta Mater* 2002;50:4021.
- [5] Marquis EA, Seidman DN, Dunand DC. *Acta Mater* 2003;51:285.
- [6] Hyland Jr RW. *Metall Mater Trans A* 1992;23:1947.
- [7] Drits MY, Ber LB, Bykov YG, Toporovan LS, Anastas'eva GK. *Phys Met Metall* 1984;57:118.
- [8] Iwamura S, Miura Y. *Acta Mater* 2004;52:591.
- [9] Fuller CB, Seidman DN, Dunand DC. *Scripta Mater* 1999;40:691.
- [10] Blake N, Hopkins MA. *J Mater Sci* 1985;20:2861.
- [11] Novotny GM, Ardell AJ. *Mater Sci Eng A: Struct Mater: Properties Microstruct Process* 2001;318:144.
- [12] Clouet E, Barbu A, Lan L, Martin G. *Acta Mater* 2005;53:2313.
- [13] Røyset J, Ryum N. *Mater Sci Eng A* 2005;396:409.
- [14] Marquis EA, Riesther JL, Seidman DN, Larson DJ. *Microsc Microanal* 2006;12:914.
- [15] Marquis EA, Seidman DN. *Acta Mater* 2005;53:4259.
- [16] Marquis EA, Seidman DN, Dunand DC. *Acta Mater* 2003;51:4751.
- [17] Marquis EA, Seidman DN, Dunand DC. In: Zin J, Beaudoin A, Bieler TA, Radhakrishnan B, editors. *Hot deformation of aluminum alloys III*. Warrendale, PA: TMS; 2003. p. 177.
- [18] Marquis EA, Seidman DN, Asta M, Woodward C, Ozolins V. *Phys Rev Lett* 2003;91:036101.
- [19] Marquis EA, Seidman DN. *Surf Interf Anal* 2004;36:559.
- [20] Marquis EA, Seidman DN, Asta M, Woodward C. *Acta Mater* 2006;54:119.
- [21] van Dalen ME, Dunand DC, Seidman DN. *J Mater Sci* 2006;41:7814.
- [22] Karnesky RA, van Dalen ME, Dunand DC, Seidman DN. *Scripta Mater* 2006;55:437.
- [23] Fuller CB, Seidman DN, Dunand DC. *Acta Mater* 2003;51:4803.
- [24] van Dalen ME, Dunand DC, Seidman DN. *Acta Mater* 2005;53:4225.
- [25] Fuller CB, Murray JL, Seidman DN. *Acta Mater* 2005;53:5401.
- [26] Fuller CB, Seidman DN. *Acta Mater* 2005;53:5415.
- [27] Harada Y, Dunand DC. *Mater Sci Forum* 2007;539–543:1565.
- [28] Sawtell RR. *Exploratory alloy development in the system Al–Sc–X*. University of California, Berkeley, CA; 1988.
- [29] Sawtell RR, Morris J. *Dispersion strengthened aluminum alloys*. Warrendale, PA: TMS; 1988. p. 409.
- [30] Harada Y, Dunand DC. *Intermetallics* 2009;17:17.
- [31] Krug ME, Werber A, Dunand DC, Seidman DN. *Acta Mater* 2010;58:134.
- [32] Wen JC, Weppner W, Boukamp BA, Huggins RA. *Metall Trans B: Process Metall* 1980;11:131.
- [33] Baumann SF, Williams DB. *Metall Mater Trans A* 1985;16:1203.
- [34] Hallstedt B, Kim O. *Int J Mater Res* 2007;98:961.
- [35] Noble B, Bray SE. *Acta Mater* 1998;46:6163.
- [36] Fujikawa S, Izeki Y, Hirano K. *Scripta Metall* 1986;20:1275.
- [37] Cocco G, Fagherazzi G, Schiffrini L. *J Appl Crystallogr* 1977;10:325–7.
- [38] Levine E, Rapperport E. *Trans Metall Soc AIME* 1963;227:1204.
- [39] Krug ME, Dunand DC, Seidman DN. *Appl Phys Lett* 2008;92:124107.
- [40] Radmilovic V, Tolley A, Marquis EA, Rossel MD, Lee Z, Dahmen U. *Scripta Mater* 2008;58:529.
- [41] Noble B, Harris S, Dinsdale K. *J Mater Sci* 1982;17:461.
- [42] Fox AG, Fisher RM. *J Mater Sci Lett* 1988;7:301.
- [43] Gasior W, Moser Z, Pstruz J. *J Phase Equilib* 1998;19:234.
- [44] Meric C. *J Mater Eng Perform* 2000;9:266.
- [45] Schmitz G, Haasen P. *Acta Metall Mater* 1992;40:2209.
- [46] Schmitz G, Hono K, Haasen P. *Acta Metall Mater* 1994;42:201.
- [47] Noble B, Bray SE. *Philos Mag A: Phys Condens Matter: Defects Mech Properties* 1999;79:859.
- [48] Miura Y, Matsui A, Furukawa M, Nemoto M. *Plastic deformation of Al–Li single crystals*. In: Baker C, Gregson PJ, Harris SJ, Peel CJ, editors. *Aluminium–lithium alloys III*. Oxford; 1986. p. 427.
- [49] Jeon SM, Park JK. *Philos Mag A: Phys Condens Matter: Defects Mech Properties* 1994;70:493.
- [50] Baumann SF, Williams DB. *Acta Metall Mater* 1985;33:1069.
- [51] Hono K, Babu SS, Hiraga K, Okano R, Sakurai T. *Acta Metall Mater* 1992;40:3027.
- [52] Messerschmidt U, Bartsch M. *Mater Sci Eng A: Struct Mater Properties Microstruct Process* 1993;164:332.
- [53] Sanders TH, Starke EA. *Acta Metall* 1982;30:927.
- [54] Williams DB. *Microstructural characteristics of aluminum–lithium alloys*. In: Sanders TH Jr., Starke EA Jr., editors. *Aluminum–lithium alloys, Proceedings of the 1st international aluminum conference*. Warrendale, PA: Metallurgical Society of AIME; 1981. p. 89.
- [55] Williams DB, Edington JW. *Met Sci* 1975;9:529–32.
- [56] Nembach E. *Prog Mater Sci* 2000;45:275–338.
- [57] Cassada WA, Shiflet GJ, Jesser WA. *Acta Metall Mater* 1992;40:2101.
- [58] Marquis EA, Seidman DN, Dunand DC. *Acta Mater* 2002;50:4021.
- [59] Miura Y, Horikawa K, Yamada K, Nakayama M. In: *Aluminum alloys: their physical and mechanical properties*, vol. 2; 1994. p. 161.
- [60] Gayle FW, Vandersande JB. *Scripta Metall* 1984;18:473.
- [61] Gayle FW, Vandersande JB. *Acta Metall Mater* 1989;37:1033.
- [62] Aydinol MK, Bor AS. *J Mater Sci* 1994;29:15.
- [63] Aydinol MK, Bor AS. *J Mater Sci* 1995;14:1147.
- [64] Knipling KE, Dunand DC, Seidman DN. *Zeitschrift für Metallkunde* 2006;97:246.
- [65] Rossel MD, Erni R, Tolley A, Marquis EA, Radmilovic V, Dahmen U. *Microsc Microanal* 2008;12:1348.
- [66] van Dalen ME, Karnesky RA, Cabotaje JR, Dunand DC, Seidman DN. *Acta Mater* 2009;57:4081.
- [67] Monachon C, Dunand DC, Seidman DN. *SMALL* 2010;6:1728.
- [68] Sato T, Kamio A. *Mater Sci Eng A: Struct Mater: Properties, Microstruct Process* 1991;146:161.
- [69] Jones W, Das P. *J I Met* 1960;88:435.
- [70] Poduri R, Chen L-Q. *Acta Metall Mater* 1996;45:245.
- [71] Marquis EA, Hyde JM. *Mater Sci Eng: R: Rep* 2010;69:37.
- [72] Seidman DN. *Ann Rev Mater Res* 2007;37:127.
- [73] Seidman DN, Stiller K. *MRS Bull* 2009;34:717.
- [74] Seidman DN, Stiller K. *MRS Bull* 2009;34:892.
- [75] Krakauer BW, Hu JG, Kuo SM, Mallick RL, Seki A, Seidman DN, et al. *Rev Sci Instrum* 1990;61:3390.
- [76] Miller MK, Kenik EA. *Microsc Microanal* 2004;10:336.
- [77] Kolli RP, Seidman DN. *Microsc Microanal* 2007;13:272.

- [78] Monachon C, Hessler-Wyser A, Faes A, Herle Jv, Tagliaferri E. *J Am Ceram Soc* 2008;91:3405.
- [79] Stadelmann P. *Microsc Microanal* 2003;9:60.
- [80] Schlesier C, Nembach E. *Mater Sci Eng A: Struct Mater: Properties, Microstruct Process* 1989;119:199.
- [81] Sudbrack CK, Noebe RD, Seidman DN. *Phys Rev B: Condens Matter Mater Phys* 2006;73:1.
- [82] Hellman OC, Vandenbroucke JA, Rüsing J, Isheim D, Seidman DN. *Microsc Microanal* 2000;6:437.
- [83] Miller MK, Forbes RG. *Mater Character* 2009;60:461.
- [84] Raho A, Kadi-Hanifi M. *Annales De Chimie-Science Des Materiaux* 2007;32:513.
- [85] Nembach E. *Particle strengthening of metals and alloys*. New York: Wiley-Interscience; 1996.
- [86] Argon A. *Strengthening mechanisms in crystal plasticity*. Oxford: Oxford University Press; 2007.
- [87] Friedel J. *Dislocations*. Oxford: Pergamon Press; 1964.
- [88] Krug ME, Dunand DC, Seidman DN. in preparation.
- [89] Knipling KE, Dunand DC, Seidman DN. *Microsc Microanal* 2007;13:1.
- [90] Marquis EA, Vurpillot F. *Microsc Microanal* 2008;14:561.
- [91] Minamino Y, Yamane T, Araki H. *Metall Trans A – Phys Metall Mater Sci* 1987;18:1536.
- [92] Porter DA, Easterling KE. *Phase transformations in metals and alloys*. Boca Raton, FL: Taylor & Francis; 2004.
- [93] Yoshi-Yama T, Mannami MH. *J Phys Soc Jpn* 1968;25:908.